Electronic Supplementary Information

Using a dual-emission Sm(III)-macrocycle as the perceptive lab-on-a-molecule chemosensor toward selective and discriminative detection of nitroaromatic explosives

Chengjian Zhang, Ruijie Zheng, Sichen Li, Kang Yang, Shengdi Tai, Yinsong Tao, Shishen Zhang and Kun Zhang*

School of Chemistry and Chemical Engineering, Key Laboratory of Surface & Interface Science of Polymer Materials of Zhejiang Province, Zhejiang Sci-Tech University, Hangzhou 310018, P. R. China

Crystal structure determination and refinement

A high-quality single-crystal sample of complex **Sm-2$_l$** was covered with glue and mounted on glass fiber for data collection. Crystallographic data were collected at 150(2) K on a Bruker SMART 1K CCD diffractometer, using graphite mono-chromated MoKα radiation (λ = 0.71073 Å). Absorption corrections were performed to all data and the structure was solved by direct method and refined by full-matrix least-squares method on F_{obs}^2 by using the SHELXTL-PC software package [1]. All non-H atoms were anisotropically refined and all hydrogen atoms were inserted in the calculated positions assigned fixed isotropic thermal parameters and allowed to ride on their respective parent atoms. A summary of the crystal data, experimental details and refinement results for **Sm-2$_l$** was listed in Table S1. Selected bond lengths and bond angles of **Sm-2$_l$** were tabulated in Table S2, and hydrogen bond parameters were shown in Table S3.

References

1 Sheldrick, G. M. SHELXTL (Version 6.10). Software Reference Manual; Madison, Wisconsin (USA): Bruker AXS, Inc.: **2000**.

Tables

Table S1 Crystal data and structural refinements for **Sm-2$_l$**.

Complex	**Sm-2$_l$**
Empirical formula	$C_{30}H_{31}BrCl_2N_5O_{10}Sm$
Formula weight	922.76
Temperature / K	293(2)
Wavelength / Å	0.71073
Crystal Size (mm)	0.14×0.21×0.26
Crystal system	Monoclinic
Space group	C2/c
a / Å	43.493(3)
b / Å	8.4563(6)
c / Å	18.8102(15)
α / °	90
β / °	93.291(2)
γ / °	90
V / Å^3	6906.8(9)
Z / D_{calcd} (g / cm^3)	8/1.775
F(000)	3656
μ / mm^{-1}	3.074
h_{min} / h_{max}	–52/56
k_{min} / k_{max}	–10/11
l_{min} / l_{max}	–24/24
Data / parameters	8050/442
R_1, wR_2 [$I > 2\sigma(I)$][a]	R_1 = 0.0406, wR_2 = 0.0803
R_1, wR_2 (all data)[a]	R_1 = 0.0730, wR_2 = 0.0906
S	1.00
Max/min $\Delta\rho$/e Å^{-3}	1.05/–0.99

[a] $R_1 = \Sigma||Fo|-|Fc|| / \Sigma|Fo|$, $wR_2 = [\Sigma[w(Fo^2-Fc^2)^2] / \Sigma w(Fo^2)^2]^{1/2}$

Table S2 Selected bond distances (Å) and angles (°) in **Sm-2$_l$**.

Bond distances		Bond angles	
Sm-2$_l$			
Sm1–O1	2.319(3)	O1–Sm1–O2	120.74(9)
Sm1–O2	2.723(3)	O1–Sm1–O3	174.83(10)
Sm1–O3	2.675(3)	O1–Sm1–O4	68.92(9)
Sm1–O4	2.355(3)	O1–Sm1–O5	116.98(10)
Sm1–O5	2.581(3)	O1–Sm1–O6	73.81(10)
Sm1–O6	2.529(3)	O1–Sm1–O8	70.53(10)

Sm1–O8	2.579(4)	O1–Sm1–O9	109.11(11)
Sm1–O9	2.499(4)	O1–Sm1–N2	66.26(10)
Sm1–N2	2.688(4)	O1–Sm1–N3	117.45(10)
Sm1–N3	2.610(3)	O2–Sm1–O3	59.43(9)
		O2–Sm1–O4	137.50(9)
		O2–Sm1–O5	70.33(10)
		O2–Sm1–O6	72.06(10)
		O2–Sm1–O8	127.18(10)
		O2–Sm1–O9	80.64(10)
		O2–Sm1–N2	62.83(10)
		O2–Sm1–N3	121.70(10)
		O3–Sm1–O4	114.76(9)
		O3–Sm1–O5	68.16(10)
		O3–Sm1–O6	110.53(10)
		O3–Sm1–O8	105.07(10)
		O3–Sm1–O9	65.72(11)
		O3–Sm1–N2	110.91(10)
		O3–Sm1–N3	62.31(10)
		O4–Sm1–O5	69.23(10)
		O4–Sm1–O6	72.17(10)
		O4–Sm1–O8	95.33(10)
		O4–Sm1–O9	138.80(11)
		O4–Sm1–N2	133.23(10)
		O4–Sm1–N3	68.55(10)
		O5–Sm1–O6	49.63(10)
		O5–Sm1–O8	156.31(11)
		O5–Sm1–O9	133.35(11)
		O5–Sm1–N2	121.65(10)
		O5–Sm1–N3	87.10(10)
		O6–Sm1–O8	144.32(11)
		O6–Sm1–O9	148.69(11)
		O6–Sm1–N2	83.17(11)
		O6–Sm1–N3	129.71(10)
		O8–Sm1–O9	49.76(11)
		O8–Sm1–N2	82.04 (11)
		O8–Sm1–N3	70.19(11)
		O9–Sm1–N2	70.68(11)
		O9–Sm1–N3	77.89(11)
		N2–Sm1–N3	147.12(11)

Table S3 Intramolecular hydrogen bond parameters (Å, °) in **Sm-2$_l$**.

D–H···A	D–H	H···A	D···A	∠DHA
Sm-2$_l$				
N1–H1···O1	0.98	1.95	2.689(4)	132
N1–H1···O4	0.98	1.98	2.769(4)	136

Table S4 Bond distances ($d_{Sm,j}$), bond valences ($v_{Sm,j}$) and total samarium atom valence (V_{Sm}) in the crystal structure of **Sm-2$_l$**.

Compound	Atom	Donor type	$d_{Sm,j}$/Å	$v_{Sm,j}$	V_{Sm}
Sm-2$_l$	N2	$HL2_l^-$	2.688	0.252	2.936
	N3	$HL2_l^-$	2.610	0.311	
	O1	$HL2_l^-$	2.319	0.495	
	O2	$HL2_l^-$	2.723	0.166	
	O3	$HL2_l^-$	2.675	0.189	
	O4	$HL2_l^-$	2.355	0.449	
	O5	NO_3^-	2.581	0.244	
	O6	NO_3^-	2.529	0.281	
	O8	NO_3^-	2.579	0.245	
	O9	NO_3^-	2.499	0.304	

Table S5 Analytical parameters of fluorescent chemosensors studied herein for detection of nitroaromatic explosives.

chemosensor	Sensing mechanism and effect	NACs	Linear range	LOD	Solvent	Reference
GCDs	FL quenching	TNP	0.1-0.15μM	0.091μM	Water	Acta A: Mol. Biomol.Spectrosc. 137 (2015) 1213
sensor 1 sensor 2	FL quenching	TNP	0-100μM	70 ppb 300ppb	CH_3CN	Anal. Chim. Acta 936 (2016) 216
PI-CONs	FL enhancement	TNP	0.5-10μM	0.25μM	EtOH	ACS Appl. Mater. Interfaces. 2017, 9,13415
$[Bi(L^1)(NO_3)]_n$ $[Bi(L^2)(NO_3)_3]$	FL quenching	2,4-DNP TNP	5-70μM 5-70μM 5-55μM 5-100μM	0.0968μM 0.0924μM	DMF	Sens. Actuators B Chem. 264 (2018) 363
$BaAlF_5:Eu^{2+}$@PEI $BaSiF_6:Eu^{2+}$@PEI	FL quenching	TNP	1-5 ng/ml 3-20 ng/ml	0.57ng/ml 2.82ng/ml	EtOH	J. Rare Earth. 39 (2021) 952
L_1 $L_1@C_b$	FL quenching	TNP	NR	29.3±3.7nM 29nM	THF	ACS Omega 5 (2020) 25747
Sensor 3 Sensor 4	FL quenching	TNP	NR	4.1nM 5.9nM	DMF	Spectrochim. Acta A. 226 (2020) 117583
Zn-MOFs 1 Zn-MOFs 2 Zn-MOFs 3 Zn-MOFs 4	FL quenching	2-NP	0-0.125mM 0-0.170 mM 0-0.120 mM 0-0.170 mM	0.79μM 1.34μM 2.98μM 0.73μM	Water	Cryst. Growth Des. 21 (2021) 5558
EY@Zr-MOF	FL quenching	2-NP	0.01-1mM	NR	EtOH	ACS Sustain. Chem. Eng. 7 (2019) 6196
$[Nd_2CdL_2(NO_3)_2(DMF)_2](OH)_2$	FL quenching	2-NP	0-640μM	14.73μM	CH_3CN	Front. Chem. 7 (2019) 139

NR = Not Reported

References

1 Z. Li, Y. Wang, Y. Ni, S. Kokot, A sensor based on blue luminescent graphene quantum dots for analysis of a common explosive substance and an industrial intermediate, 2,4,6-trinitrophenol, *Acta A: Mol. Biomol. Spectrosc.* 2015, **137**, 1213−1221.

2 C. Wu, J.-L. Zhao, X.-K. Jiang, X.-L. Ni, X. Zeng, C. Redshaw, T. Yamato, Click-modified hexahomotrioxacalix[3]arenes as fluorometric and colorimetric dual-modal chemosensors for 2,4,6-trinitrophenol, *Anal. Chim. Acta* 2016, **936,** 216−221.

3 C. L. Zhang, S. M. Zhang, Y H. Yan, F. Xia, A. Huang, Y. Z. Xian, Highly fluorescent polyimide covalent organic nanosheets as sensing probes for the detection of 2,4,6-trinitrophenol, *ACS Appl. Mater. Inter.* 2017, **9**, 13415−13421.

4 O. Gungor, M. Kose, Selective detections of nitroaromatic explosives by monomeric and polymeric Bi(III) complexes, *Sensor. Actuat. B-Chem.* 2018, **264**, 363−371.

5 X. Zhang, L. T. Liu, W. Zhang, L. Y. Na, R. Hua, Detection of 2,4,6-trinitrophenol based on f-f transition of Eu^{2+}, *J. Rare Earth.* 2021, **39**, 952−958.

6 A. Narula, M. A. Hussain, A. Upadhyay, C. P. Rao, 1,3-Di-naphthalimide conjugate of Calix[4]arene as a sensitive and selective sensor for trinitrophenol and this turns reversible when hybridized with carrageenan as beads, *ACS Omega* 2020, **5**, 25747−25756.

7 F. Qiu, Y.-H. Huang, Q. M. Ge, M. Liu, H. Cong, Z. Tao, The high selective chemo-sensors for TNP based on the mono- and di-substituted multifarene[2,2] with different fluorescence quenching mechanism, *Spectrochim. Acta A.* 2020, **226**, 117583.

8 W. B. Liu, N. Li, X. Zhang, Y. Zhao, Z. Zong, R. X. Wu, J. P. Tong, C. F. Bi, F. Shao, Y. h. Fan, Four Zn(II)-MOFs as highly sensitive chemical sensor for the rapid detection of tetracycline, o-nitro phenol, $Cr_2O_7^{2-}$/PO_4^{3-}, Fe^{3+}/Al^{3+} in water environment, *Cryst. Growth Des.* 2021, **21**, 5558−5572.

9 Y. K. Li, Z. H. Wei, Y. Zhang, Z. F. Guo, D. S. Chen, P. Y. Jia, P. Chen, H. Z. Xing, Dual-emitting EY@Zr-MOF composite as self-calibrating luminescent sensor for selective detection of inorganic ions and nitroaromatics, *ACS Sustain. Chem. Eng.* 2019, **7**, 6196−6203.

10 H. F. Chen, X. P. Yang, W. Z. Jiang, D. M. Jiang, D. L. Shi, B. C. Yuan, F. Wang, L. J. Zhang, S. M. Huang, Anion dependent self-assembly of polynuclear Cd-Ln Schiff base nanoclusters: NIR luminescent sensing of nitro explosives, *Front. Chem.* 2019, **7**, 139.

Figures

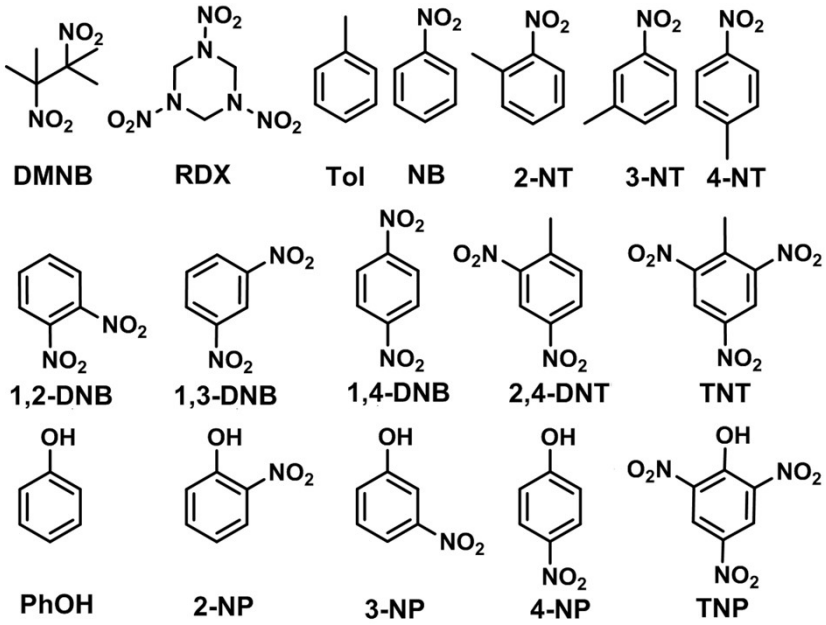

Fig. S1 Analogues of nitroaromatic explosives discussed in this work.

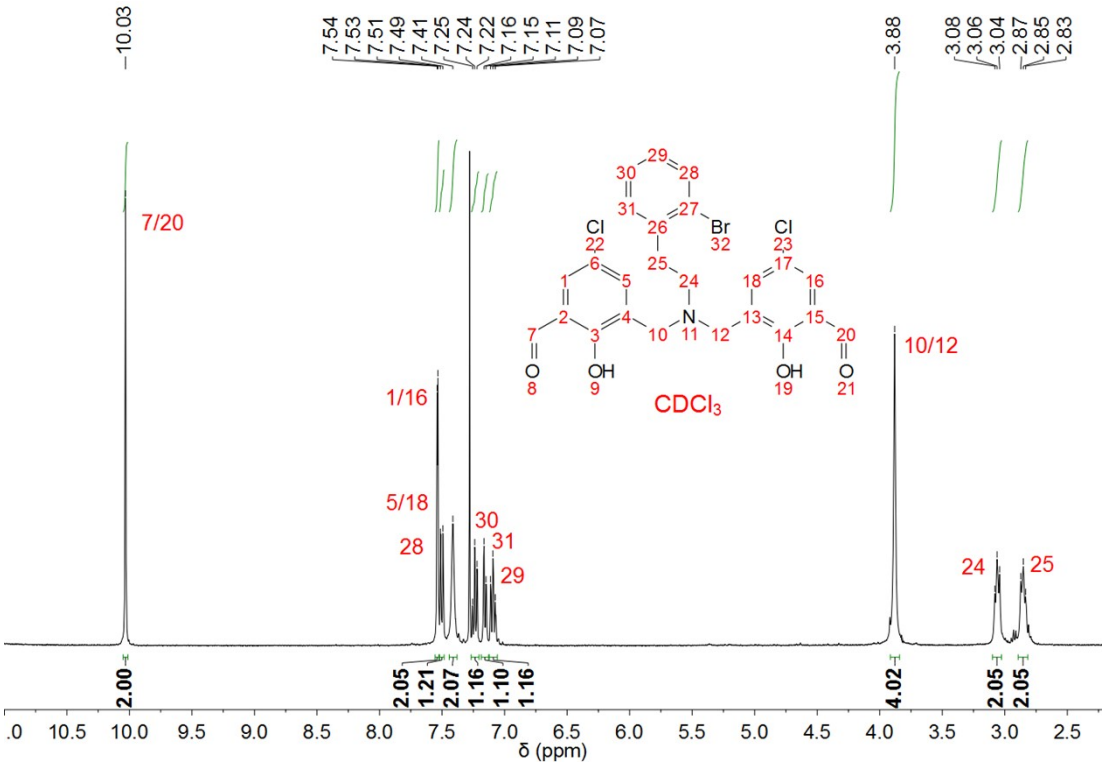

Fig. S2 ^{1}H NMR spectrum of dialdehyde H_2Q_I in $CDCl_3$.

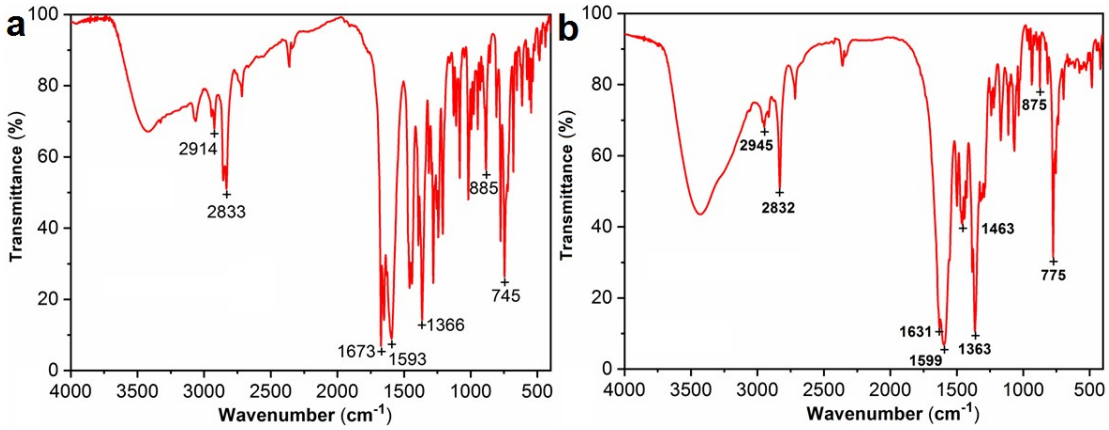

Fig. S3 FT-IR spectrum of dialdehyde H_2Q_I (a) and Sm(III)-macrocycle **Sm-2**$_I$ (b).

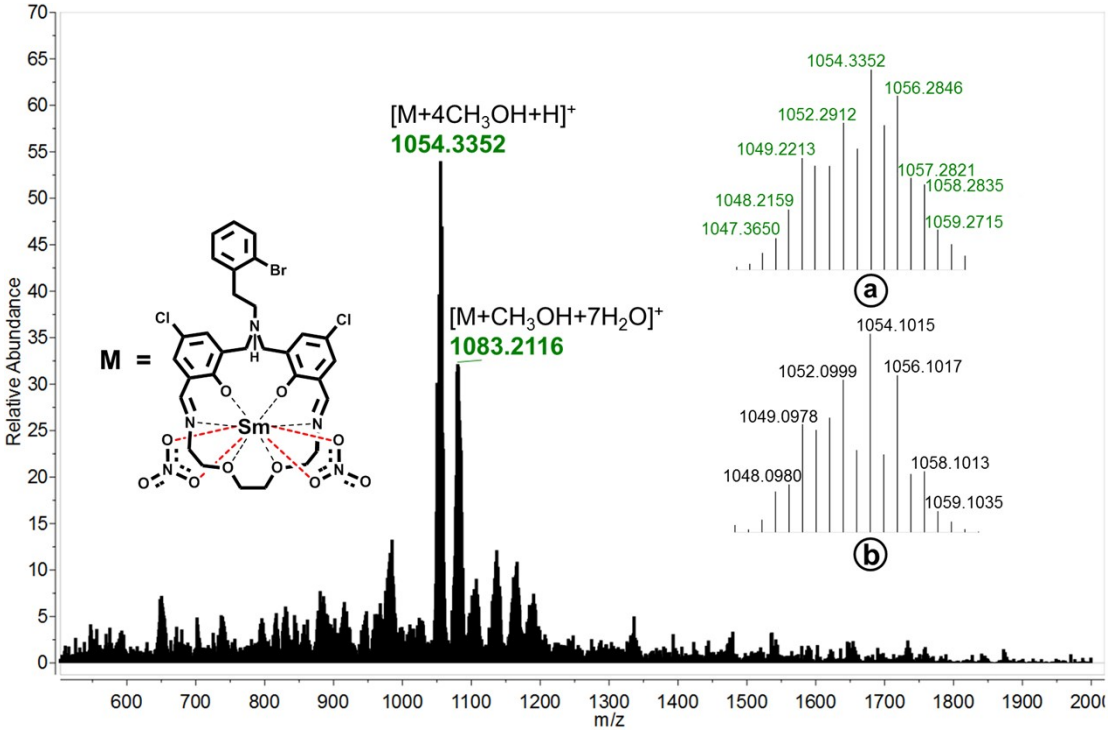

Fig. S4 ESI-MS (positive) of Sm(III)-macrocycle **Sm-2**$_I$ together with its inserted experimental (a) and simulative (b, calculation for $[C_{34}H_{48}BrCl_2N_5O_{14}Sm]$) peaks of isotopic distribution corresponding to the peak at m/z = 1054.3352.

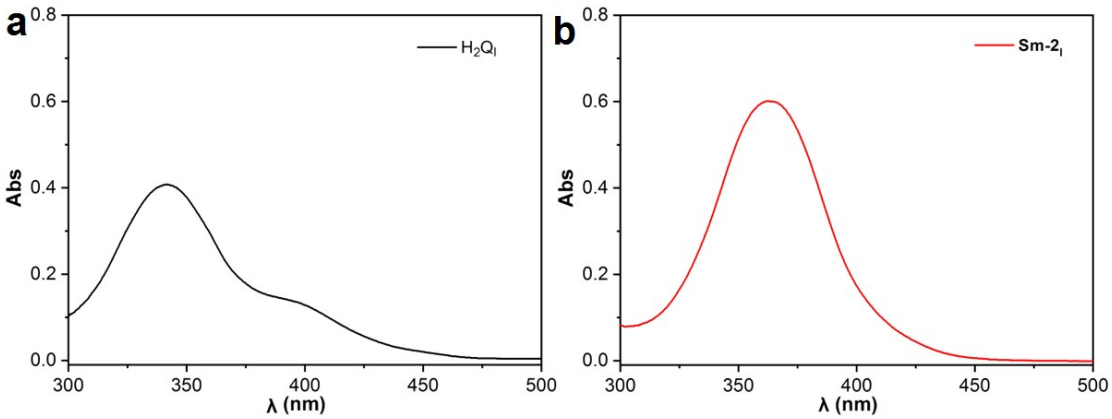

Fig. S5 UV-vis spectra of H_2Q_I (a, 40.0 μM) and **Sm-2$_I$** (b, 45.0 μM) in DMF.

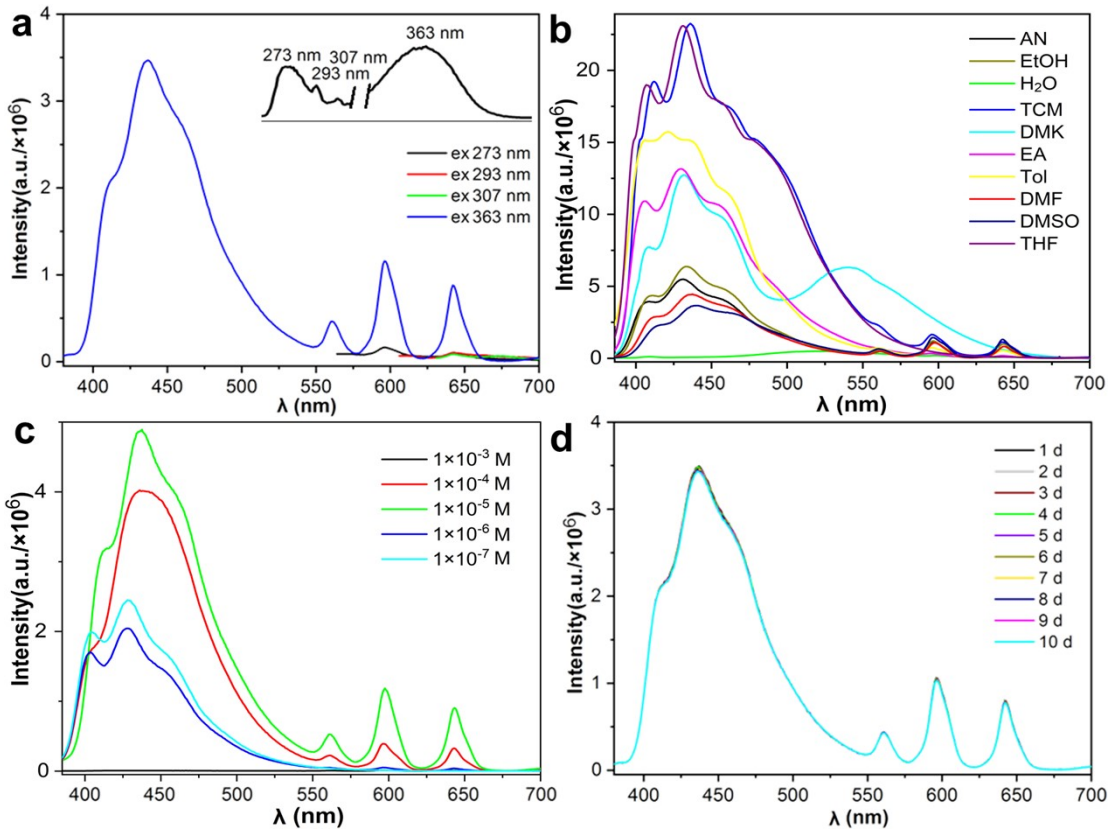

Fig. S6 (a) Emission spectra (λ_{ex} = 273, 293, 307 and 363 nm) of **Sm-2$_I$** (30.0 μM) in DMF-H_2O (19:1, *v*/*v*). Inset: Excitation spectra of **Sm-2$_I$** (λ_{em} = 643 nm, black line). (b) Emission spectra (λ_{ex} = 363 nm) of **Sm-2$_I$** (25.0 μM) in 10 common solvents. (c) Emission spectra (λ_{ex} = 363 nm) of **Sm-2$_I$** at different concentrations in DMF-H_2O (19:1, *v*/*v*) and citric acid-sodium citrate buffer (pH = 6.0, 5.00 mM). (d) Time-dependent emission spectra of **Sm-2$_I$** (30.0 μM) in DMF-H_2O (19:1, *v*/*v*) at 298 K.

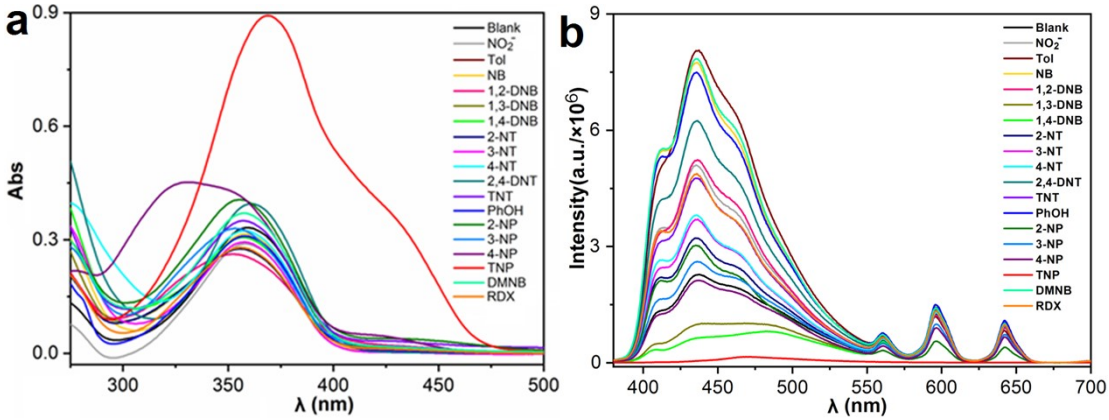

Fig. S7 Absorption (a) and fluorescence (b) spectra of **Sm-2**$_l$ (25.0 μM) mixed with explosives (125.0 μM) in DMF-H_2O (19:1, *v*/*v*) and citric acid-sodium citrate buffer (pH = 6.0, 5.00 mM).

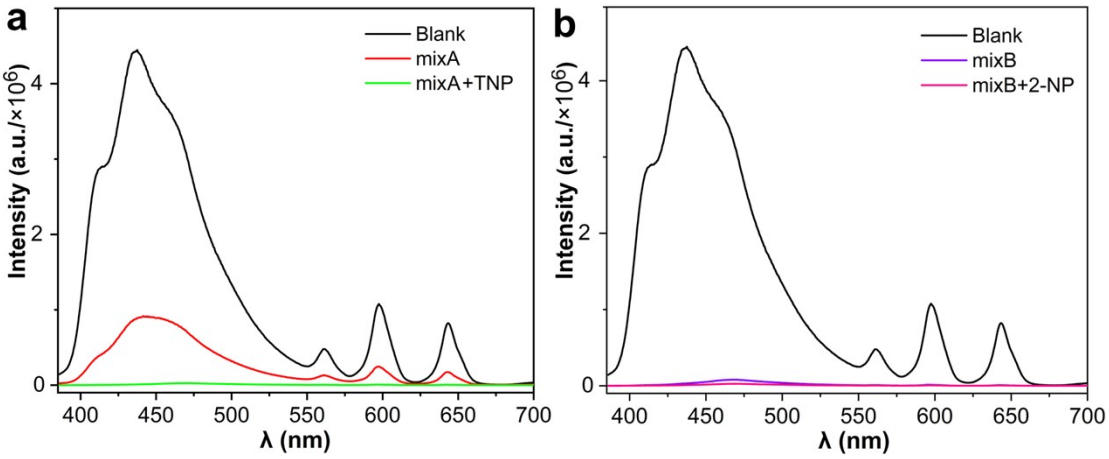

Fig. S8 Emission spectra (λ_{ex} = 363 nm) of different mixtures contained **Sm-2**$_l$ (25.0 μM) in DMF-H_2O (19:1, *v*/*v*). (mixA: mixture of 17 explosive analogues without TNP, mixB: mixture of 17 explosive analogues without 2-NP)

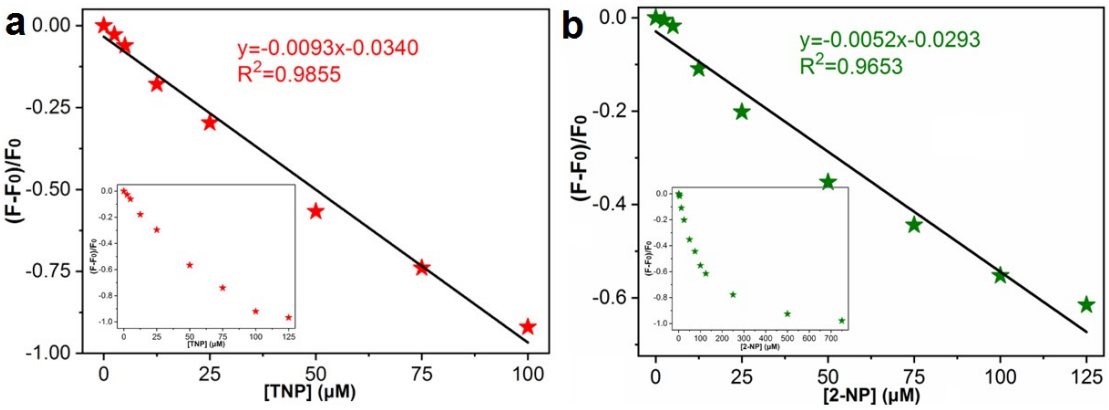

Fig. S9 Fluorescence changes of **Sm-2**$_l$ (25.0 μM) upon increasing TNP (a, 0–125.0 μM), 2-NP (b, 0–750.0 μM) (λ_{em} = 643 nm) versus the concentration of NEs in DMF-H_2O (19:1, *v*/*v*) and citric acid-sodium citrate buffer (pH = 6.0, 5.00 mM) at 298 K.

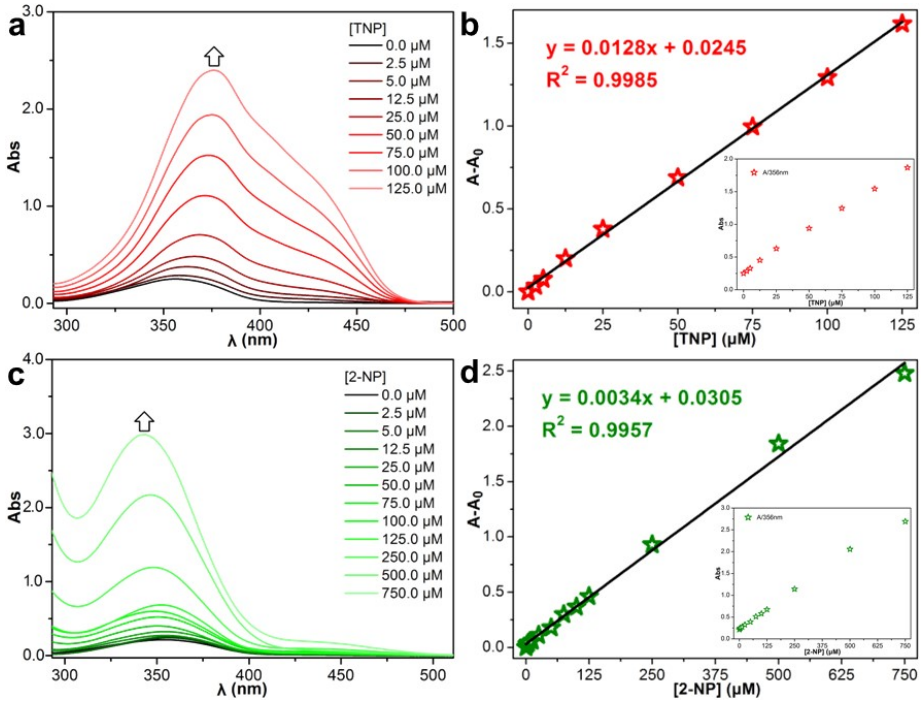

Fig. S10 Absorption changes of **Sm-2**$_I$ (25.0 μM) upon increasing contents of TNP (a, 0−125.0 μM), 2-NP (c, 0−750.0 μM) together with the inserted linearity of absorbance (360nm) versus the concentration of NEs in DMF-H_2O (19:1, *v*/*v*) and citric acid-sodium citrate buffer (pH = 6.0, 5.00 mM) at 298 K.

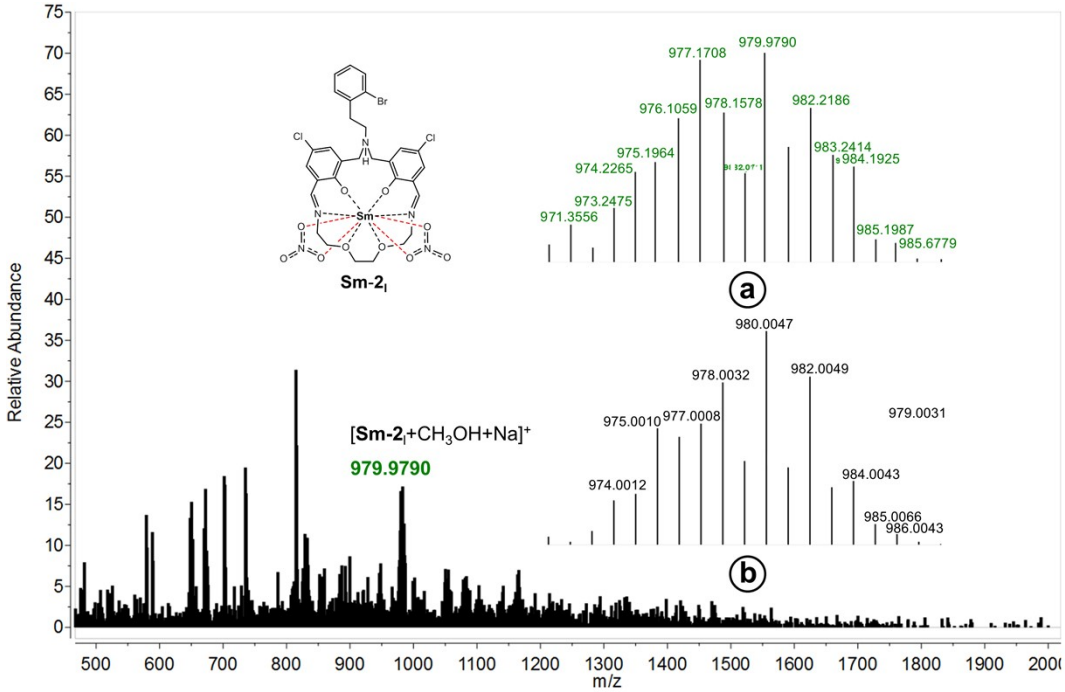

Fig. S11 ESI-MS (positive) of Sm(III)-macrocycle **Sm-2**$_I$ (25.0 μM) mixed with TNP (125.0 μM) together with its inserted experimental (a) and simulative (b, calculation for [$C_{31}H_{35}BrCl_2N_5NaO_{11}Sm$]) peaks of isotopic distribution corresponding to the peak at m/z = 979.9790.

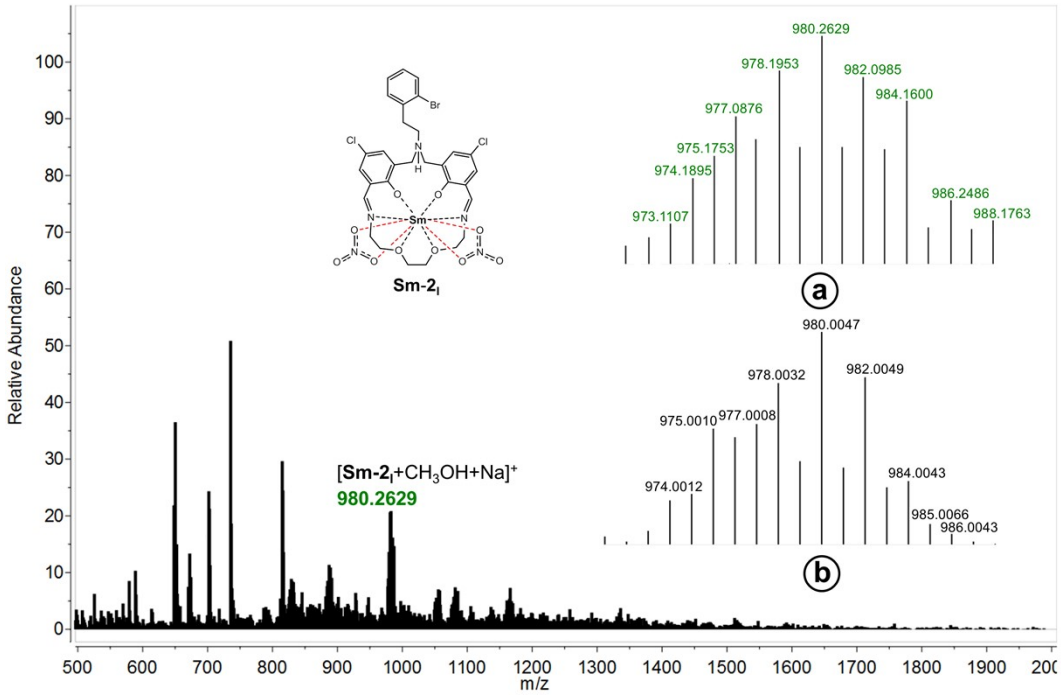

Fig. S12 ESI-MS (positive) of Sm(III)-macrocycle **Sm-2**$_I$ (25.0 μM) mixed with 2-NP (125.0 μM) together with its inserted experimental (a) and simulative (b, calculation for [$C_{31}H_{35}BrCl_2N_5NaO_{11}Sm$]) peaks of isotopic distribution corresponding to the peak at m/z = 980.2629.

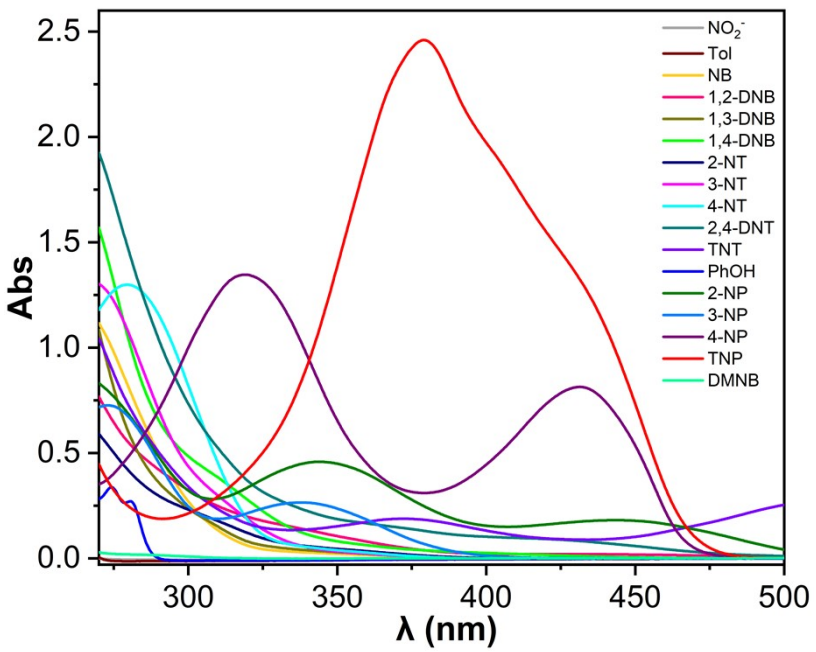

Fig. S13 Absorption spectra of explosive analogues (125.0 μM) in DMF-H_2O (19:1, *v*/*v*).

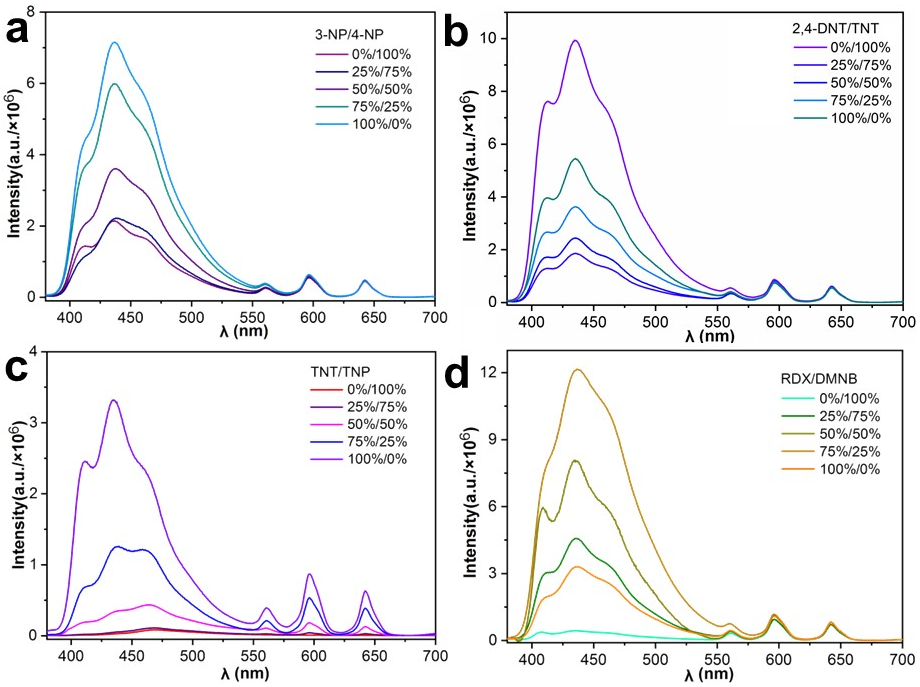

Fig. S14 Emission spectra of **Sm-2**$_l$ (25.0 μM) under the presence of serial two-component mixtures: 3-NP/4-NP (a), 2,4-DNT/TNT (b), TNT/TNP (c), and RDX/DMNB (d) in DMF-H_2O (19:1, *v*/*v*) and citric acid-sodium citrate buffer (pH = 6.0, 5.00 mM) at 298 K. For mixtures, we set up a series of five contents (0%, 25%, 50%, 75% and 100%) for one component.

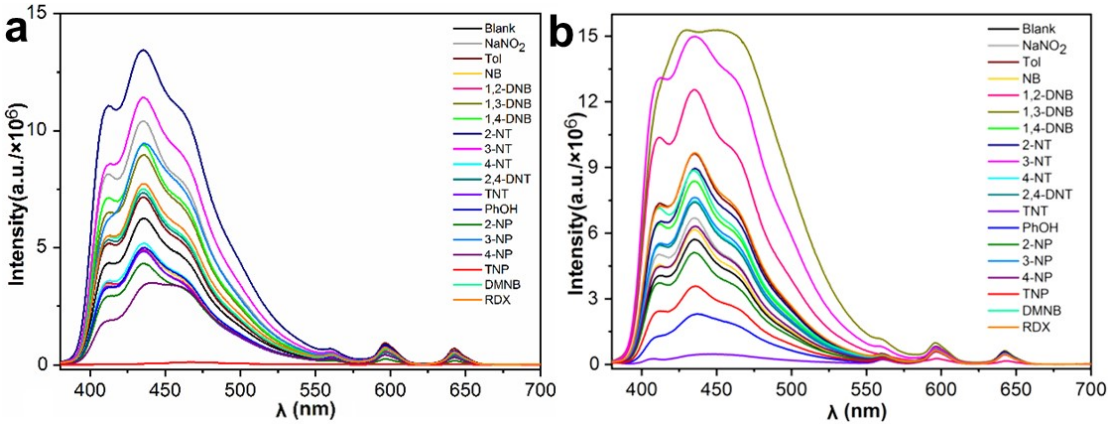

Fig. S15 Fluorescence spectra of **Sm-2**$_l$ mixed with different contents of explosives (a, 125.0 μM; b, 2.5 μM) in real water samples.